

Boundary-Driven Complex Brillouin Zone in Non-Hermitian Electric Circuits

Yung Kim,^{1,2,*} Sonu Verma,^{3,*} Minwook Kyung,^{1,*} Kyungmin Lee,¹
Wenwen Liu,⁴ Shuang Zhang,⁴ Bumki Min,^{1,2,†} and Moon Jip Park^{5,‡}

¹*Department of Physics, Korea Advanced Institute of Science and Technology, Daejeon 34141, Republic of Korea*

²*Department of Mechanical Engineering, Korea Advanced Institute of Science and Technology, Daejeon 34141, Republic of Korea*

³*Center for Theoretical Physics of Complex Systems,*

Institute for Basic Science, Daejeon 34126, Republic of Korea

⁴*Department of Electrical and Electronic Engineering, University of Hong Kong, Hong Kong, China*

⁵*Department of Physics, Hanyang University, Seoul 04763, Republic of Korea*

Complex-valued physical quantities, often non-conserved, represent key phenomena in non-Hermitian systems such as dissipation and localization. Recent advancements in non-Hermitian physics have revealed boundary-condition-sensitive band structures, characterized by a continuous manifold of complex-valued momentum known as the generalized Brillouin zone (GBZ). However, the ability to actively manipulate the GBZ and its associated topological properties has remained largely unexplored. Here, we demonstrate a controllable manipulation of the GBZ by adjusting the boundary Hamiltonian and leveraging the boundary sensitivity in a circuit lattice. Our observations reveal that the GBZ forms multiple separated manifolds containing both decaying and growing wave functions, in contrast to the previously observed non-Hermitian skin effect under open boundary condition (OBC). By continuously deforming the GBZ, we observe the topological phase transitions of innate topological structure of GBZ that are enriched by complex properties of non-Hermitian physical variables. Notably, such topological phase transition is governed by boundary conditions rather than bulk properties, underscoring the extreme boundary sensitivity unique to non-Hermitian systems.

Controlling the spatiotemporal propagation of waves is a fundamental interest in many areas of physics [1–5]. Recently, non-Hermitian systems have shown distinguished properties for this purpose, exhibiting highly sensitive band structures that respond to boundary conditions [6–11]. This pronounced boundary sensitivity is a universal feature of wave phenomena, spanning classical to quantum systems, and is observed in platforms such as photonic [12–15], acoustic [16–19], circuit [20–26], and mechanical systems [27–29], as well as ultracold atomic gases [30, 31].

Non-Hermiticity extends the real-valued momentum of the Brillouin zone (BZ) into a complex manifold, known as the generalized Brillouin zone (GBZ) under OBC [6, 32–34]. Given that boundary conditions in non-Hermitian systems are not limited to periodic or open forms [35–37], the introduction of a continuously deformable boundary Hamiltonian allows a feasible approach to engineering non-Hermitian band structures without a holistic change to the system [38–40]. Here, we propose a circuit lattice with tunable boundary components as a promising framework for investigating boundary-sensitive phenomena in non-Hermitian systems (Fig. 1(a)). We demonstrate experimentally that deforming the boundary Hamiltonian not only reshapes the morphology of the GBZ manifold but also induces changes in its topological structure, revealing a deep interplay be-

tween boundary conditions and system topology.

Consider the scattering matrix approach that relates the incoming and outgoing waves as they interact with the scattering source:

$$\Psi_{\text{out},k} = \hat{S}_{kk'} \Psi_{\text{in},k'}, \quad (1)$$

where $\Psi_{\text{out(in)},k}$ are the amplitude of incoming (outgoing) wave functions with momentum k . Eq. (1) encodes the symmetry of the physical systems. For instance, in time-reversal symmetric medium, the scattering matrix is symmetric, $\hat{S} = \hat{S}^T$. With non-Hermiticity, scattering matrix is generally non-unitary, $\hat{S}^\dagger \hat{S} \neq I$, indicating the eigenvalues can extend outside the unit circle in the complex plane.

Eq.(1) also describes the lattice model with the boundary terms. For instance, in Hatano-Nelson (HN) model [41] with a boundary, the wave packets with distinct momenta are coupled by the scattering matrix as,

$$\begin{bmatrix} |\Psi_{\text{R}}(z_1)\rangle \\ |\Psi_{\text{L}}(z_2)\rangle \end{bmatrix} = \begin{bmatrix} T_{11} & R_{12} \\ R_{21} & T_{22} \end{bmatrix} \begin{bmatrix} |\Psi_{\text{L}}(z_1)\rangle \\ |\Psi_{\text{R}}(z_2)\rangle \end{bmatrix}, \quad (2)$$

where $|\Psi_{\text{L(R)}}(z)\rangle$ is the wave function of the left (right) side respect to the boundary. The complex momentum is written as, $z = e^{ik}$. Here, we denote $z_1 = e^{ik}$ and $z_2 = e^{-ik}$, which define the forward and backward wave propagation, respectively. Therefore, T_{ij} and R_{ij} with

* These authors contributed equally to this work.

† bmin@kaist.ac.kr

‡ moonjipark@hanyang.ac.kr

$i, j \in \{1, 2\}$ are the transmission and reflection amplitudes, respectively. The relation between scattering matrix theory and non-Bloch band theory is illustrated in supplementary material (SM).

Our circuit system is designed to emulate the non-Hermitian lattice model with tunable boundary Hamiltonian. The current-voltage response of the circuit system is given as, $\mathbf{I} = \hat{J}\mathbf{V}$, where \hat{J} is the admittance matrix (or circuit Laplacian) [42]. Here, \mathbf{I} and \mathbf{V} represent the vector components of the input current and the output node voltage response, respectively. \hat{J} plays a role of the tight-binding Hamiltonian, where this correspondence enables direct access to physical information about the eigenstate and eigenvalue spectrum [43]. This allows us to extract the eigenvalues of \hat{J} through measurements of the admittance spectrum and voltage distributions across circuit nodes.

The circuit Laplacian is composed of the bulk and the controllable boundary term as, $\hat{J} = \hat{J}_{\text{bulk}} + \hat{J}_{\text{bdy}}$ (Fig. 1a-d):

$$J_{\text{bulk}} = \sum_{n=2}^{N-1} 2C_1 |n\rangle\langle n| + \sum_{n=1}^N \left(C_g - \frac{1}{\omega^2 L_g} \right) |n\rangle\langle n| + \sum_{n=1}^{N-1} (C_L |n\rangle\langle n+1| + C_R |n+1\rangle\langle n|) \quad (3)$$

and

$$J_{\text{bdy}} = \mu_1 |1\rangle\langle 1| + \mu_N |N\rangle\langle N| - C'_R |N\rangle\langle 1| - C'_L |1\rangle\langle N|, \quad (4)$$

where C_R and C_L represent the coupling capacitances corresponding to the right and left hopping amplitudes between bulk nodes, C_g and L_g represent the capacitance and inductance for the ground resonance of each node. At the boundary nodes, the onsite potentials are defined as $\mu_1 = C_L + t_b C_R + \varepsilon_1$ and $\mu_N = C_R + t_b C_L + \varepsilon_N$. The boundary coupling capacitances are $C'_R = t_b C_R$ and $C'_L = t_b C_L$, which represent the non-reciprocal hopping amplitudes between the boundary nodes. Here, $\varepsilon_{1,N}$ and t_b are boundary parameters that can be modified using adjustable switches. Each node in the circuit is connected through capacitors in parallel with an operational amplifier, also known as negative impedance converter with current inversion (INIC [44]), enabling non-reciprocal hopping amplitudes. The detailed derivation of the circuit Laplacian is provided in the SM.

The non-reciprocal hopping causes the GBZ to deviate from the unit circle, forming contours that satisfy $z_1 z_2 = t_R/t_L$ (OBC in Fig. 1e), where t_L and t_R are the hopping amplitude for the left and right direction. Under OBC, this deviation of the GBZ from the unit circle signifies macroscopic boundary localization, commonly referred to as the non-Hermitian skin effect. However, when the boundary hopping is

not fully terminated—referred to here as generalized boundary conditions (GBC)—we observe the formations of the separated manifold in the GBZs, a feature absent in both periodic boundary conditions (PBC) and OBC. The resulting eigenstates can be expressed as a linear combination of wave packets with distinct complex momenta and radii, as follows:

$$|\Psi\rangle = c_1 |\Psi(z_1)\rangle + c_2 |\Psi(z_2)\rangle, \quad (5)$$

where $|z_1| \neq |z_2|$. The non-Hermitian nature of the system, specifically non-reciprocal hopping, causes a unidirectional propagation. Consequently, in the presence of boundary scatterers, the system exhibits wave packets with transmission probability ($|T_{ii}|^2$ in Eq. 2) differing from unity. These states define the separation of manifolds in the GBZs as shown in the left panels of Fig. 1e.

Fig. 1e illustrates the eigenstates in the case of GBCs compared to OBC. Due to the separated GBZ, the eigenstates exhibit accumulated envelopes on both the left and right sides of the boundary. Microscopically, finite hopping between boundary sites enables the coexistence of left- and right-evanescent waves. This bidirectional localization of the eigenstates at the boundaries arises from the interplay between the non-Hermitian skin effect and boundary conditions. While non-reciprocal hopping alone drives wave accumulation at one edge (the non-Hermitian skin effect), the introduction of finite boundary potentials or modified boundary couplings creates additional localized states that overlap with the skin modes, giving rise to bidirectional boundary localization. In the absence of non-reciprocal hopping, the boundary term can trap at most two bound states at the boundary, similar to typical bound states in Hermitian systems [45]. On the other hand, the presence of non-reciprocal hopping allows the non-orthogonality of the eigenstates, which allows for the macroscopic accumulation of states at the boundary and localization across more than two sites. The separated GBZ possesses inherent topological structures [38]. The coupled momenta in Eq. (5) can be recast into an effective spinor form, $\psi_n(z_1, z_2) = c_1 z_1^n + c_2 z_2^n$, which includes a well-defined relative phase, $\phi = \arg(c_2/c_1)$, between the two wave components. The meromorphic function c_2/c_1 is determined by the two boundary equations $c_2/c_1 = 1/h_B^\pm(z_1, z_2) = h_B^-(z_1, z_2)$. It is related to the reflection and transmission coefficients in Eq. 2 as (c_1, c_2) determines the amplitudes of incoming and outgoing wave packets [see Eq. (5) and SM]. Therefore, a well-defined phase of c_2/c_1 allows for the definition of a winding number, which serves as the topological invariant of the GBZ:

$$W = \frac{W_+ - W_-}{2}, \quad W_\pm = \frac{1}{2\pi} [\arg(h_B^\pm(z_1, z_2))]_{\mathcal{L}_1 \times \mathcal{L}_2}, \quad (6)$$

here $\mathcal{L}_1 \times \mathcal{L}_2$ indicates the continuous contour of the GBZs satisfying $z_1 z_2 = t_R/t_L$. $\arg[h_B^\pm(z_1, z_2)]_{\mathcal{L}_1 \times \mathcal{L}_2}$ is the change of phase of $h_B^\pm(z_1, z_2)$ as (z_1, z_2) goes along the GBZ. The nontrivial winding number manifests the emergence of topological boundary modes, as illustrated in Fig. 1e. Eq. (5) can be interpreted as an effective spinor representation of the wave functions analogous to the SSH model, where the incoming and outgoing wave functions (or wave packets) play the role of the effective sublattice degrees of freedom.

To experimentally reconstruct the GBZ, we employ the wave function projection method by projecting the eigenstates of the system onto the complex plane using a complex Fourier transform (See SM). By tuning the boundary parameters $t_b, \varepsilon_{1,N}$ using 8 way dip switches (See SM), we observe the corresponding topological phase transitions, marked by the appearance or disappearance of the topological boundary modes. In the nontrivial phase, the topological boundary mode appears as distinct, separated from the complex manifolds of the bulk momenta. In contrast, in the trivial phase, both GBC and OBC exhibit only bulk modes with no topological boundary modes. As the GBZ undergoes the topological phase transition, the complex momenta of the boundary state are absorbed into the bulk spectrum. This absorption coincides with an exceptional point (EP), directly indicating the coalescence of the wave functions. Notably, this coalescence differs from the energy band touchings, as energy degeneracy does not necessarily imply the coalescence of eigenstates.

Figure 2a-d presents a comprehensive analysis of how boundary parameters, t_b and ε , influence the topological properties and the corresponding physical manifestations in our system. Here, ε is defined as $\varepsilon \equiv \varepsilon_1 = 0.5\varepsilon_N$ to clearly reveal phase transitions. It is important to note that the parameters used in these calculations are retrieved from the measured circuit Laplacian, ensuring consistency between theory and experiments. In Fig. 2a, the non-Bloch winding number W serves as a topological invariant, characterizing the system's topological phases, while the number of bound states in Fig. 2b directly corresponds to the emergence of topological boundary modes, a key observable in our setup. Additionally, the phase rigidity R in Fig. 2c quantifies the biorthogonality of the eigenstates and the inverse participation ratio (IPR) in Fig. 2d indicates the localization strength of the eigenstates. Notably, figures 2a-d reveal distinct topological phase regions in the boundary parameter space, clearly demonstrating the critical role of boundary matrix in determining topological phases.

The occurrence of topological phase transitions at EPs is one of the key features of our system. At these critical points, the GBZs make contact, resulting in the coalescence of eigenstates. Unlike conventional energy band touchings in Hermitian systems, this merging of eigenstates at EPs leads to a distinct class of non-equilibrium phase transitions, known as exceptional

transitions [46]. This phenomenon can be quantitatively identified through the phase rigidity, which measures the biorthogonality of eigenstates:

$$R_i = \frac{\langle \psi_i^R | \psi_i^L \rangle}{\langle \psi_i^R | \psi_i^R \rangle} \quad \text{for } i = 1, 2, \dots, N. \quad (7)$$

Here, $|\psi_i^{R(L)}\rangle$ denotes the right (left) eigenstate. Figure 2c maps the average phase rigidity $(R_1 + R_2 + R_{N-1} + R_N)/4$ for topological boundary states, showing that it approaches zero at topological phase transition points, providing a clear signature of exceptional transitions. To quantify the boundary localization of topological boundary states, we use the IPR [7]:

$$\text{IPR}_i = \frac{\sum_{\mathbf{r}} |\psi_i(\mathbf{r})|^4}{(\sum_{\mathbf{r}} |\psi_i(\mathbf{r})|^2)^2} \quad \text{for } i = 1, 2, \dots, N. \quad (8)$$

and Fig. 2d illustrates the IPR of topological states with the color gradient indicating the degree of eigenstate localization. This analysis reveals that topological states of the GBZ exhibit boundary localization, similar to conventional topological states. Furthermore, Fig. 2h shows an inverse relationship between the localization of topological boundary states in real space and their spread in the complex momentum space. As these states become more localized in real space, their distribution in the complex momentum space widens correspondingly (See SM).

Figure 2g shows a comparison of theoretically calculated and experimentally measured GBZs. Despite the presence of disorder in the circuit lattice such as parasitic values in lumped elements and imperfection of fabrication, the peaks in the experimental GBZ still closely align with the theoretical predictions, confirming the robustness of the GBZ topology even in the presence of moderate disorder. Figure 2h presents the experimentally measured GBZ under both OBC (upper panels) and GBC (lower panels). The distribution peaks in the GBZ align well with our theoretical predictions.

In order to present quantitative evidence for the occurrence of topological phase transitions, we demonstrate the direct measurements of the phase rigidity and IPR of the topological boundary states. Figure 2e,f illustrate these experimental results under GBC and OBC. For GBC, we fixed the ε and varied t_b (yellow dashed line in Fig. 2b). Conversely, for OBC, we fixed $t_b = 0$ and adjusted the ε (white line in Fig. 2b). In both boundary conditions, we observed two significant dips in the phase rigidity plot corresponding to the EPs shown in Fig. 2c. Although phase rigidity did not reach zero due to system size limitations, it approached values near zero, indicating the proximity to EPs. Furthermore, under the same physical conditions, the IPR of the topological boundary states approached 1, signifying strong boundary localization. These observations collectively support the occurrence of topological phase transitions in our system. The

specific boundary parameters used here are provided in Section C of the SM.

In addition to the Hatano-Nelson model, we implement the non-reciprocal next nearest-neighbor (NNN) hopping by implementing additional INICs with capacitors C_R and C_L at each node. As shown in Fig. 3a, these extra couplings replicate the same magnitude as NN couplings to realize the NNN hoppings. Details of circuit Laplacian are provided in SM. In the presence of the NNN hoppings, the bulk equation for the momenta is given as quartic equation of momentum, $t_{2L}z^4 + t_{1L}z^3 - Ez^2 + t_{1R}z + t_{2R} = 0$, here $t_{1R}(t_{1L})$ and $t_{2R}(t_{2L})$ denotes the nearest neighbor right (left) and next nearest neighbor right (left) hopping amplitudes, respectively. In general, the bulk equation has four generalized momenta solutions z_i , $i = 1, 2, 3, 4$, and the resulting eigenstates are given by:

$$|\Psi\rangle = c_1|\Psi(z_1)\rangle + c_2|\Psi(z_2)\rangle + c_3|\Psi(z_3)\rangle + c_4|\Psi(z_4)\rangle, \quad (9)$$

where z_i, c_i , $i = 1, 2, 3, 4$ are determined self-consistently by solving bulk and boundary equations. The introduction of NNN hoppings not only reveals a more complicated topological structure of the GBZ, but also leads to multiple topological states under GBC and OBC as shown in Fig. 3b [34]. The experimentally measured GBZs for trivial and nontrivial phases under GBC and OBC are shown in Fig. 3c-f. Our theoretical model reveals a complicated structure, but in practical experiments, particularly when employing Fourier transform,

only the most prominent peaks are present. This leads to the manifestation of distinctive, simplified patterns in the complex plane, a phenomenon clearly illustrated in Fig. 3c-f. Note that the topological boundary states, as observed in both real and complex planes, demonstrate behaviors parallel to those found in nearest-neighbor (NN) models. This resemblance implies that the localization properties in NN and long-range hopping models share fundamental characteristics in the context of the intrinsic topology of GBZ.

To summarize, we have demonstrated the manipulation of the GBZ using non-Hermitian scatterers and visualize its topological structure within a non-Hermitian circuit system. While several studies have examined spectral changes in the OBC of the non-Hermitian skin effect, here we find that, by precisely controlling the boundary Hamiltonian, the two momenta form separate manifolds, extending the scope of engineering the GBZ manifold in a controllable fashion, retaining the relative phase and amplitude information between the two manifolds. To further generalize our understanding of GBZ topology, we introduce next-nearest-neighbor hopping into the system. This extension leads to the observation of multiple topological boundary modes within the complex momentum space, enriching our understanding of non-Hermitian topological systems. Our findings provide the much-needed experimental evidence that the observed phenomena stem from the intrinsic topological properties of the GBZ itself, bridging the gap between theory and practice, and opening new avenues for investigating and manipulating topological properties in non-Hermitian materials.

-
- [1] P. R. Villeneuve and S. Fan, Photonic crystals, *Solid State Communications* **102**, 165 (1997).
- [2] P. Russell, Photonic crystal fibers, *science* **299**, 358 (2003).
- [3] T. Ozawa, H. M. Price, A. Amo, N. Goldman, M. Hafezi, L. Lu, M. C. Rechtsman, D. Schuster, J. Simon, O. Zeitlinger, and I. Carusotto, Topological photonics, *Rev. Mod. Phys.* **91**, 015006 (2019).
- [4] Y. Yang, B. Yang, G. Ma, J. Li, S. Zhang, and C. Chan, Non-abelian physics in light and sound, *Science* **383**, eadf9621 (2024).
- [5] I. Žutić, J. Fabian, and S. Das Sarma, Spintronics: Fundamentals and applications, *Rev. Mod. Phys.* **76**, 323 (2004).
- [6] S. Yao and Z. Wang, Edge states and topological invariants of non-hermitian systems, *Phys. Rev. Lett.* **121**, 086803 (2018).
- [7] V. M. Alvarez, J. B. Vargas, and L. F. Torres, Non-hermitian robust edge states in one dimension: Anomalous localization and eigenspace condensation at exceptional points, *Physical Review B* **97**, 121401 (2018).
- [8] K. Zhang, Z. Yang, and C. Fang, Universal non-hermitian skin effect in two and higher dimensions, *Nature communications* **13**, 2496 (2022).
- [9] J. C. Budich and E. J. Bergholtz, Non-hermitian topological sensors, *Physical Review Letters* **125**, 180403 (2020).
- [10] K. Ding, C. Fang, and G. Ma, Non-hermitian topology and exceptional-point geometries, *Nature Reviews Physics* **4**, 745 (2022).
- [11] S. Longhi, Non-hermitian skin effect and self-acceleration, *Phys. Rev. B* **105**, 245143 (2022).
- [12] S. Weidemann, M. Kremer, T. Helbig, T. Hofmann, A. Stegmaier, M. Greiter, R. Thomale, and A. Szameit, Topological funneling of light, *Science* **368**, 311 (2020).
- [13] L. Xiao, T. Deng, K. Wang, G. Zhu, Z. Wang, W. Yi, and P. Xue, Non-hermitian bulk–boundary correspondence in quantum dynamics, *Nature Physics* **16**, 761 (2020).
- [14] Y. Sun, X. Hou, T. Wan, F. Wang, S. Zhu, Z. Ruan, and Z. Yang, Photonic floquet skin-topological effect, *Phys. Rev. Lett.* **132**, 063804 (2024).
- [15] L. Xiao, W.-T. Xue, F. Song, Y.-M. Hu, W. Yi, Z. Wang, and P. Xue, Observation of non-hermitian edge burst in quantum dynamics, *Phys. Rev. Lett.* **133**, 070801 (2024).
- [16] L. Zhang, Y. Yang, Y. Ge, Y.-J. Guan, Q. Chen, Q. Yan, F. Chen, R. Xi, Y. Li, D. Jia, S.-Q. Yuan, H.-X. Sun, H. Chen, and B. Zhang, Acoustic non-hermitian skin effect from twisted winding topology, *Nature Communications* **12**, 6297 (2021).
- [17] L. Zhang, Y. Yang, Y. Ge, Y.-J. Guan, Q. Chen, Q. Yan, F. Chen, R. Xi, Y. Li, D. Jia, *et al.*, Acoustic non-

- hermitian skin effect from twisted winding topology, *Nature communications* **12**, 6297 (2021).
- [18] Q. Zhou, J. Wu, Z. Pu, J. Lu, X. Huang, W. Deng, M. Ke, and Z. Liu, Observation of geometry-dependent skin effect in non-hermitian phononic crystals with exceptional points, *Nature Communications* **14**, 4569 (2023).
- [19] Z. Gu, H. Gao, H. Xue, J. Li, Z. Su, and J. Zhu, Transient non-hermitian skin effect, *Nature Communications* **13**, 7668 (2022).
- [20] T. Helbig, T. Hofmann, S. Imhof, M. Abdelghany, T. Kiessling, L. Molenkamp, C. Lee, A. Szameit, M. Greiter, and R. Thomale, Generalized bulk–boundary correspondence in non-hermitian topoelectrical circuits, *Nature Physics* **16**, 747 (2020).
- [21] H. Zhou and B. Zhang, Topological sensing and imaging, *Nature Reviews Physics* **3**, 480 (2021).
- [22] K. Ochkan, R. Chaturvedi, V. Könye, L. Veyrat, R. Giraud, D. Mailly, A. Cavanna, U. Gennser, E. M. Hankiewicz, B. Büchner, et al., Non-hermitian topology in a multi-terminal quantum hall device, *Nature Physics* **20**, 395 (2024).
- [23] H. Yuan, W. Zhang, Z. Zhou, W. Wang, N. Pan, Y. Feng, H. Sun, and X. Zhang, Non-hermitian topoelectrical circuit sensor with high sensitivity, *Advanced Science* **10**, 2301128 (2023).
- [24] P. Zhu, X.-Q. Sun, T. L. Hughes, and G. Bahl, Higher rank chirality and non-hermitian skin effect in a topoelectrical circuit, *Nature communications* **14**, 720 (2023).
- [25] J. Wu, Z. Wang, Y. Biao, F. Fei, S. Zhang, Z. Yin, Y. Hu, Z. Song, T. Wu, F. Song, et al., Non-abelian gauge fields in circuit systems, *Nature Electronics* **5**, 635 (2022).
- [26] Y. Hadad, J. C. Soric, A. B. Khanikaev, and A. Alu, Self-induced topological protection in nonlinear circuit arrays, *Nature Electronics* **1**, 178 (2018).
- [27] W. Wang, X. Wang, and G. Ma, Non-hermitian morphing of topological modes, *Nature* **608**, 50 (2022).
- [28] A. Ghatak, M. Brandenbourger, J. van Wezel, and C. Coulais, Observation of non-hermitian topology and its bulk–edge correspondence in an active mechanical metamaterial, *Proceedings of the National Academy of Sciences* **117**, 29561 (2020).
- [29] H. Schomerus, Nonreciprocal response theory of non-hermitian mechanical metamaterials: Response phase transition from the skin effect of zero modes, *Phys. Rev. Res.* **2**, 013058 (2020).
- [30] Q. Liang, D. Xie, Z. Dong, H. Li, H. Li, B. Gadway, W. Yi, and B. Yan, Dynamic signatures of non-hermitian skin effect and topology in ultracold atoms, *Phys. Rev. Lett.* **129**, 070401 (2022).
- [31] C. Wang, N. Li, J. Xie, C. Ding, Z. Ji, L. Xiao, S. Jia, Y. Hu, and Y. Zhao, Observation of an exceptional nexus in ultracold atoms, arXiv preprint arXiv:2309.09625 (2023).
- [32] K. Yokomizo and S. Murakami, Non-bloch band theory of non-hermitian systems, *Phys. Rev. Lett.* **123**, 066404 (2019).
- [33] K. Zhang, Z. Yang, and C. Fang, Correspondence between winding numbers and skin modes in non-hermitian systems, *Phys. Rev. Lett.* **125**, 126402 (2020).
- [34] Z. Yang, K. Zhang, C. Fang, and J. Hu, Non-hermitian bulk-boundary correspondence and auxiliary generalized brillouin zone theory, *Phys. Rev. Lett.* **125**, 226402 (2020).
- [35] C.-X. Guo, C.-H. Liu, X.-M. Zhao, Y. Liu, and S. Chen, Exact solution of non-hermitian systems with generalized boundary conditions: size-dependent boundary effect and fragility of the skin effect, *Physical Review Letters* **127**, 116801 (2021).
- [36] P. Mognini, O. Arandes, and E. J. Bergholtz, Anomalous skin effects in disordered systems with a single non-hermitian impurity, *Phys. Rev. Res.* **5**, 033058 (2023).
- [37] F. Roccati, Non-hermitian skin effect as an impurity problem, *Phys. Rev. A* **104**, 022215 (2021).
- [38] S. Verma and M. J. Park, Topological phase transitions of generalized brillouin zone, *Communications Physics* **7**, 21 (2024).
- [39] C.-X. Guo, L. Su, Y. Wang, L. Li, J. Wang, X. Ruan, Y. Du, D. Zheng, S. Chen, and H. Hu, Scale-tailored localization and its observation in non-hermitian electrical circuits, *Nature Communications* **15**, 9120 (2024).
- [40] L. Li, C. H. Lee, and J. Gong, Impurity induced scale-free localization, *Communications Physics* **4**, 42 (2021).
- [41] N. Hatano and D. R. Nelson, Localization transitions in non-hermitian quantum mechanics, *Physical review letters* **77**, 570 (1996).
- [42] C. H. Lee, S. Imhof, C. Berger, F. Bayer, J. Brehm, L. W. Molenkamp, T. Kiessling, and R. Thomale, Topoelectrical circuits, *Communications Physics* **1**, 39 (2018).
- [43] T. Helbig, T. Hofmann, C. H. Lee, R. Thomale, S. Imhof, L. W. Molenkamp, and T. Kiessling, Band structure engineering and reconstruction in electric circuit networks, *Phys. Rev. B* **99**, 161114 (2019).
- [44] T. Hofmann, T. Helbig, C. H. Lee, M. Greiter, and R. Thomale, Chiral voltage propagation and calibration in a topoelectrical chern circuit, *Phys. Rev. Lett.* **122**, 247702 (2019).
- [45] X.-L. Qi and S.-C. Zhang, Topological insulators and superconductors, *Reviews of modern physics* **83**, 1057 (2011).
- [46] M. Fruchart, R. Hanai, P. B. Littlewood, and V. Vitelli, Non-reciprocal phase transitions, *Nature* **592**, 363 (2021).

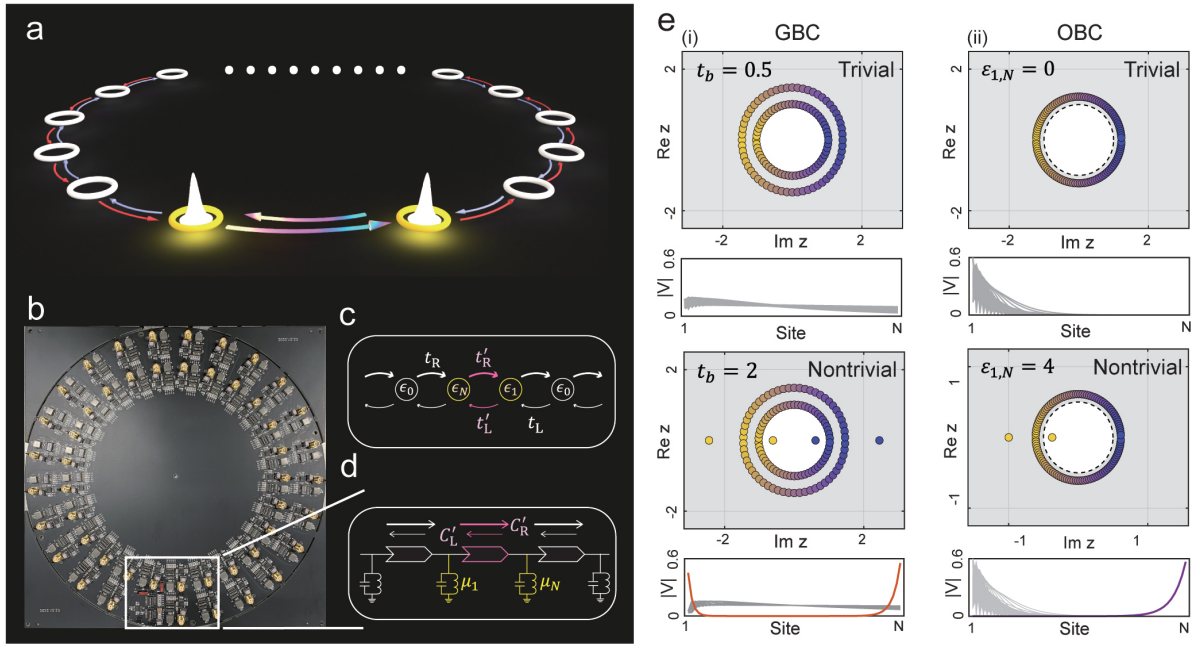


FIG. 1. **Hatano-Nelson circuit with generalized boundary.** **a** Schematic illustration of the one-dimensional non-Hermitian HN model with GBZ. **b** Photograph of the implemented printed circuit board (PCB). **c** Tight-binding model of our system. The parameters ε_0, t_R, t_L represent onsite potential, hopping amplitudes for right and left direction of bulk sites. $\varepsilon_1, \varepsilon_N, t'_R, t'_L$ denote the boundary onsite potentials and hopping amplitudes. **d** Corresponding circuit model. Non-reciprocal hoppings are realized by INICs. At the boundary, we implemented tunable switches to change the onsite potentials C'_g, L'_g and hopping amplitudes C'_R, C'_L . **e** Topological phase transition of GBZ under GBC (i) and OBC (ii). The topological phase transition occurred depending on the changes of onsite potential and coupling amplitude, leading to the appearance of topological boundary modes in complex and real space simultaneously. Note that onsite potentials are fixed at $\varepsilon_{1,N} = 0$ under GBC.

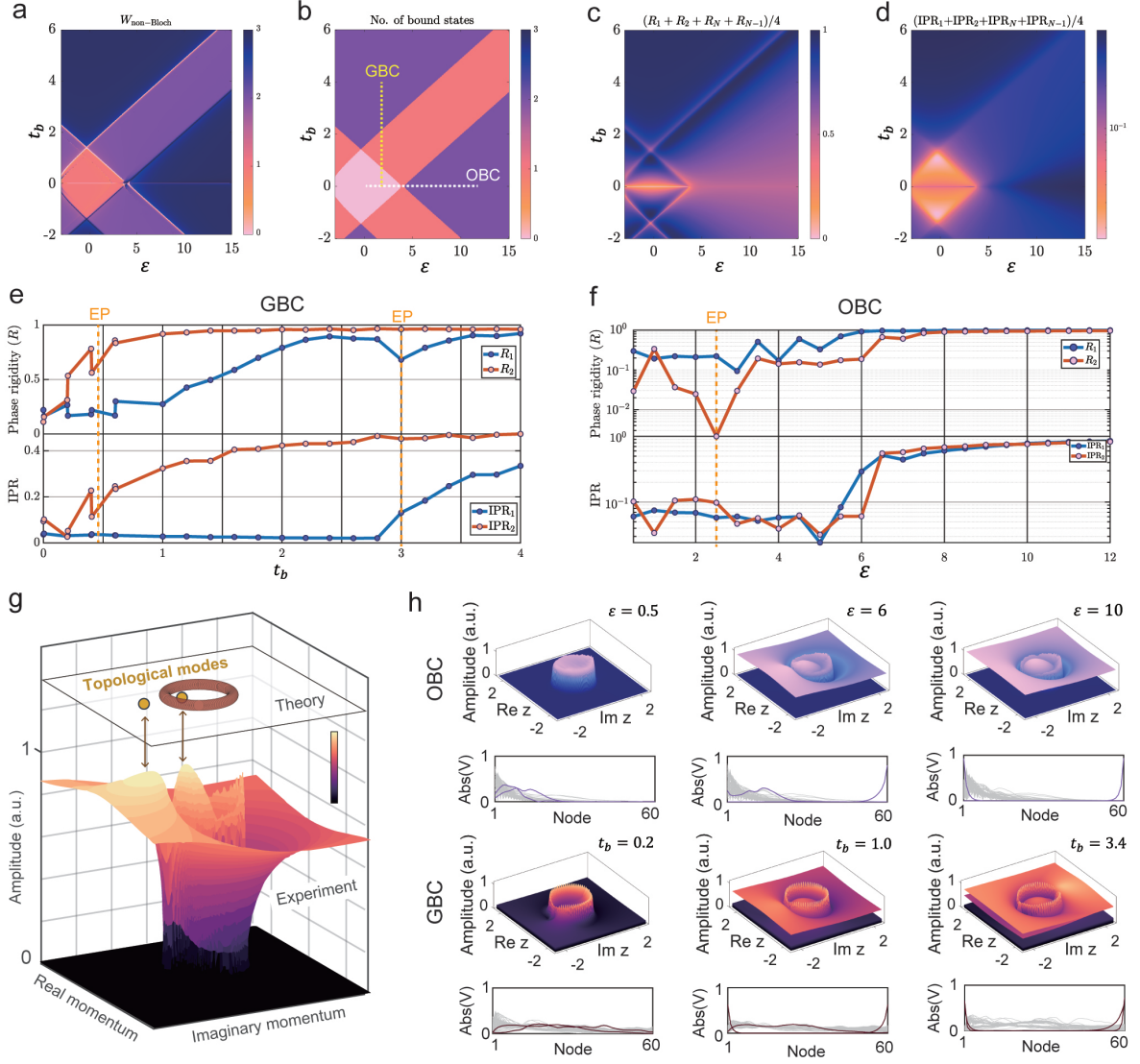


FIG. 2. **Intrinsic topology of GBZ.** **a-d** Phase diagram of non-Bloch winding number, number of boundary states, phase rigidity, and IPR as a function of boundary parameters. **e,f** Phase rigidity (top) and IPR (bottom) as a function of t_b and ϵ under GBC **e** and OBC **f**. The appearance of EP corresponds to abrupt changes in both the phase rigidity and IPR, indicating topological phase transitions. **g** Comparison between theoretically (clean) calculated and experimentally measured (disordered) GBZ. **h** Experimentally measured GBZs and corresponding eigenstate distributions under OBC (top row) and GBC (bottom row) for different boundary parameters. The emergence of topological states is clearly visualized in complex and real space.

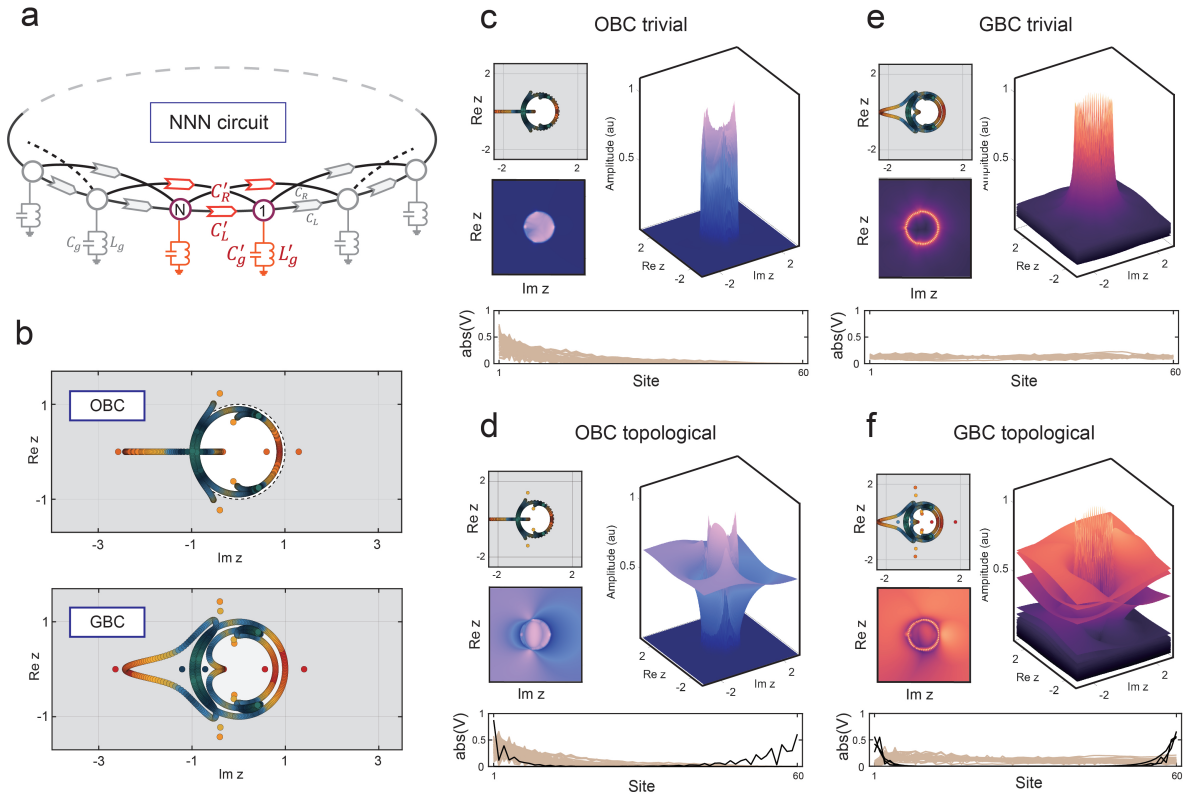


FIG. 3. **Topological phase transition of GBZ in complex plane for NNN case.** **a** Sketch of the next-nearest-neighbor (NNN) circuit model, showing additional long-range coupling components (INICs). **b** Theoretical calculation of GBZ under OBC (blue) and GBC for NNN model. In topological phase, multiple topological boundary states appear at complex plane. **c-f** GBZ structure of NNN model and corresponding eigenstate distributions. For each case, top-left panel shows the theoretical data and bottom-left panel displays a top view of measured GBZ. The right panel presents a 3D visualization of the measured GBZ structure, and the bottom panel shows the eigenstate distribution across lattice sites.